*Supplementary Information for*

# A BPDF database retrieved using multi-angle, multispectral and polarimetric observations from POLDER-3 and DPC-2

Zhe Ji[1,2], Zhengqiang Li[1,2,3*], Gerrit de Leeuw[1,4], Cheng Chen[5], Yahui Che[6], Zihan Zhang[1], Luo Zhang[7]

[1]State Key Laboratory of Remote Sensing and Digital Earth & Key Laboratory of Satellite Remote Sensing of Ministry of Ecology and Environment, Aerospace Information Research Institute, Chinese Academy of Sciences, Beijing 100101, China.
[2]University of Chinese Academy of Sciences, Beijing 100049, China.
[3]State Key Laboratory of Spatial Datum, College of Remote Sensing and Geoinformatics Engineering, Faculty of Geographical Science and Engineering, Henan University, Zhengzhou, 450046, China.
[4]Royal Netherlands Meteorological Institute (KNMI), R&D Satellite Observations, P.O.Box 201, 3730AE De Bilt, The Netherlands.
[5]Anhui Institute of Optics and Fine Mechanics, Hefei Institutes of Physical Science, Chinese Academy of Sciences, Hefei 230031, China.
[6]Institute for Atmospheric Physics, Chinese Academy of Sciences, Beijing 100029, China.
[7]Satellite Application Center for Ecology and Environment, Ministry of Ecology and Environment, Beijing 100094, China.

**S1. Sensitivity of polarized atmospheric path reflectance to aerosol-model assumptions**

To evaluate the sensitivity of the polarized atmospheric path reflectance used in atmospheric correction to aerosol-model selection under low-aerosol-loading conditions, six aerosol models were selected from the global aerosol classification developed by Omar et al. (2005) through cluster analysis of AERONET radiance measurements and inversion-derived aerosol properties. The six aerosol types included polluted continental, biomass burning, clean continental/background, polluted marine, dirty pollution, and desert dust. These six models were used only to evaluate sensitivity to aerosol-model selection and did not replace the continental aerosol model adopted for database construction.

Polarized atmospheric path reflectance was calculated for the six aerosol models at a fixed $AOD_{550}$ of 0.10. The fixed $AOD_{550}$ of 0.10 represents the upper boundary of the low-aerosol-loading range examined in this study. The calculations covered four solar zenith angles (SZA; 8.0, 28.7, 49.3, and 70.0°), five relative azimuth angles (RAA; 8, 51, 94, 137, and 180°), and 40 viewing zenith angles (VZAs) ranging from 0 to 60°. The same 800 observation geometries were used for each aerosol model and wavelength. Fixing AOD and observation geometry allowed the differences in polarized path reflectance associated with aerosol-model selection to be evaluated without interference from variations in aerosol loading or angular sampling.

At 490 nm, the polarized path reflectances simulated using the six aerosol models are closely grouped over most of the sampled angular domain (Figure S1). The differences are particularly small at low and moderate SZAs. At SZA = 70°, some separation among the models becomes visible at larger VZAs, although the inter-model spread remains limited relative to the magnitude of the polarized path reflectance. Aerosol-model selection therefore has a relatively small influence on the simulated polarized path reflectance at 490 nm under most of the geometries examined.

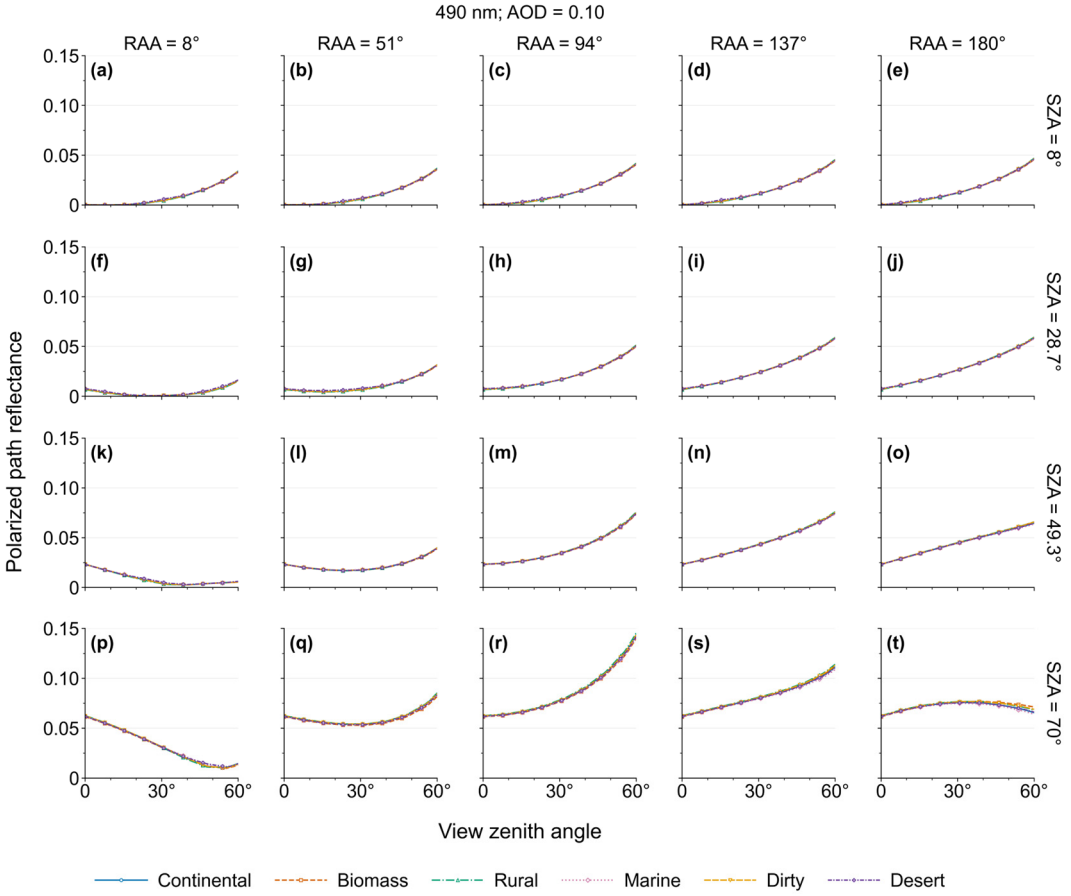



Figure S1. Polarized atmospheric path reflectance simulated at 490 nm using six aerosol models at $AOD_{550}$ = 0.10.

At 670 nm, the magnitude of the polarized path reflectance is lower than at 490 nm, while the relative separation among the aerosol models becomes more apparent under some observation geometries (Figure S2). The model curves remain closely grouped at low SZAs but diverge progressively as SZA increases. The largest differences occur mainly at SZA = 70°, particularly for larger RAAs and oblique viewing directions. The relative ordering of the aerosol models also varies with observation geometry, indicating that the effect of aerosol-model selection cannot be represented by a single geometry-independent offset.

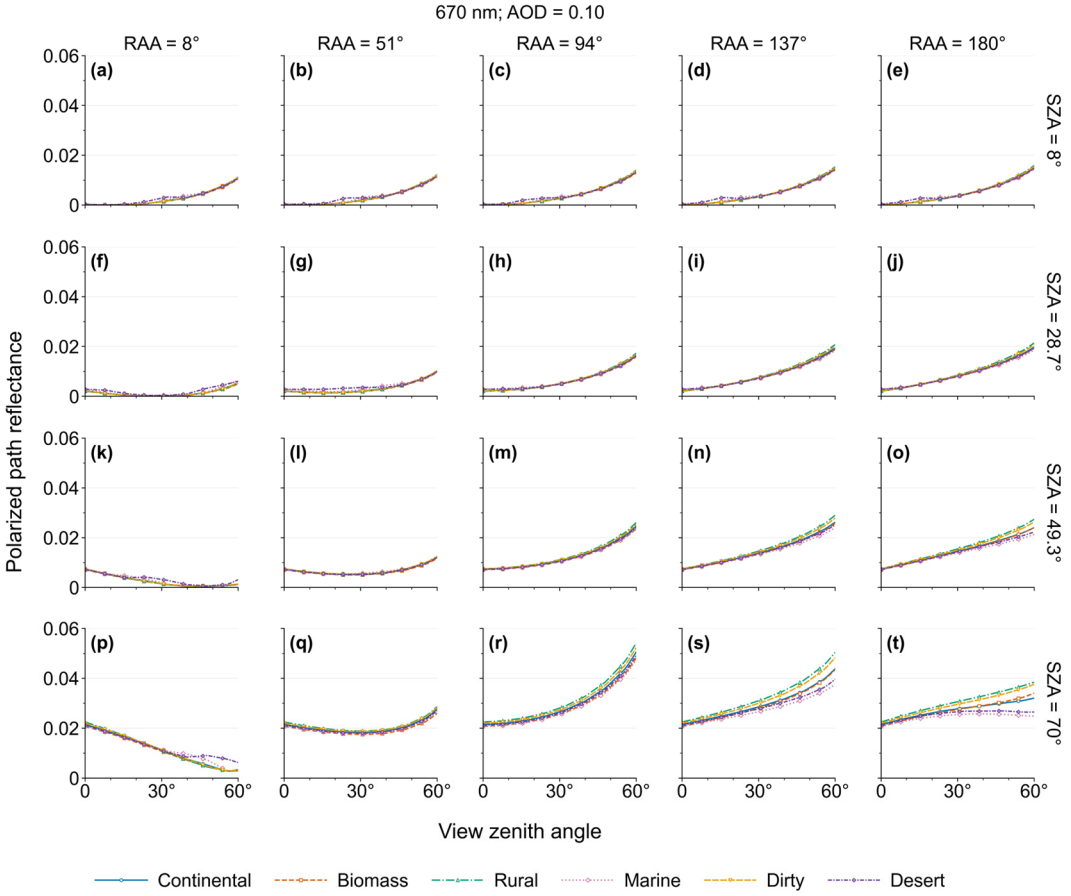



Figure S2. Polarized atmospheric path reflectance simulated at 670 nm using six aerosol models at $AOD_{550}$ = 0.10.

At 865 nm, the polarized path reflectance is lower still, but its relative sensitivity to the prescribed aerosol model becomes more pronounced (Figure S3). The inter-model spread is largest at high SZA, large RAA, and large VZA, particularly at SZA = 70° and RAA values between 94 and 180°. Localized differences among the models are also evident under several low- and moderate-SZA geometries. As at 670 nm, the relative ordering of the models changes across the angular domain, demonstrating that model sensitivity depends on the specific combination of illumination and viewing geometry.

Taken together, Figs. S1–S3 show that differences among the six aerosol models are limited over much of the sampled angular domain at $AOD_{550}$=0.10, but become non-negligible under large-SZA and oblique-viewing conditions. The relative separation among the models is generally more apparent at 670 and 865 nm than at 490 nm. Aerosol-model sensitivity therefore depends on both wavelength and observation geometry. This analysis quantifies the sensitivity of simulated polarized atmospheric path reflectance to aerosol-model selection under the tested conditions. It does not quantify atmospheric-correction errors against an independent reference.

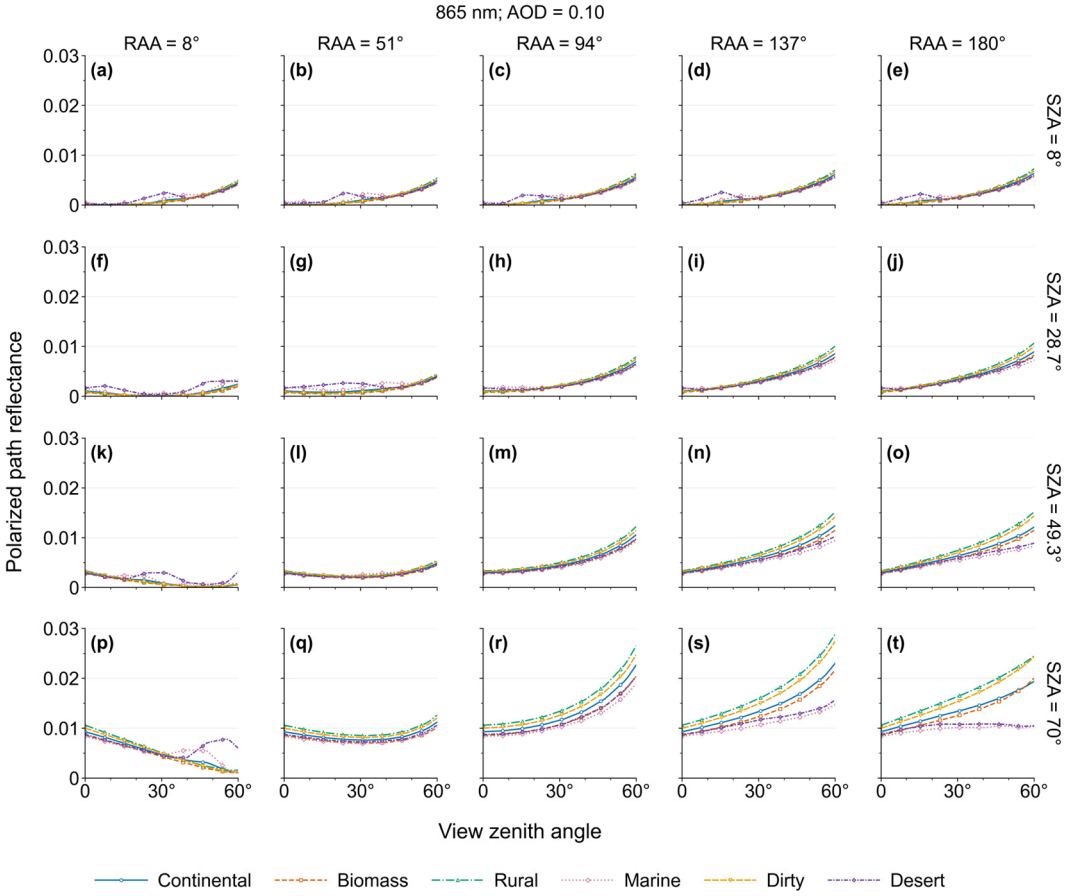



Figure S3. Polarized atmospheric path reflectance simulated at 865 nm using six aerosol models at $AOD_{550}$ = 0.10.

## S2. Spectral fusion of surface polarized reflectance

A band-specific $R_p$ was considered valid when $0 \leq R_p \leq 1$. At least two valid bands were required to calculate the fused $R_p$. The default weights for 490, 670, and 865 nm were:

$$w_{490}: w_{670}: w_{865} = 1: 2: 3 \quad (S1)$$

Let $B_i$ denote the subset of the 490, 670, and 865 nm bands retained for the fusion of direction i according to the procedure described in Sect. S2. The weighted least-squares estimate, which is equivalent to the following weighted mean, was initially calculated as:

$$R_{p,i} = \frac{\sum_{b \in B_i} w_b R_{p,b,i}}{\sum_{b \in B_i} w_b} \quad (S2)$$

When all three bands passed the validity screening, their median $m_i$ was first calculated, followed by the median absolute deviation:

$$\mathrm{MAD_i} = \mathrm{median}\left|R_{\mathrm{p,b,i}} - m_{\mathrm{i}}\right| \quad (S3)$$

The corresponding robust scale was then calculated as:

$$s_{\mathrm{i}} = 1.4826 \times \mathrm{MAD_i} \quad (S4)$$

The normalized discrepancy of band b was:

$$z_{\mathrm{b,i}} = \frac{\left|R_{\mathrm{p,b,i}} - R_{\mathrm{p,i}}\right|}{s_{\mathrm{i}}} \quad (S5)$$

When all three bands were valid and the maximum normalized discrepancy exceeded 3.5, the single band with the largest discrepancy was excluded. The fused $R_{\mathrm{p}}$ was then recalculated from the retained bands after renormalizing their weights. Directions with fewer than two valid bands were assigned a missing fused value. The final fused $R_{\mathrm{p}}$ represents the surface polarization signal jointly constrained by the retained bands and does not correspond to an individual wavelength..

## S3. Quality assurance (QA) criteria and class assignment

### S3.1 Primary QA thresholds

Because all observations retained in the databases satisfy $AOD_{550} < 0.1$, the aerosol-loading component was assigned $QA_3$ for every retained observation. Table S1 lists the thresholds for the four components that vary within the database. Surface homogeneity and angular sampling are assigned to each multi-angle sequence, whereas SZA and VZA are assigned to individual viewing directions.

Table S1. Thresholds used to assign the QA component grades

| Component | $QA_3$ | $QA_2$ | $QA_1$ | $QA_0$ |
|---|---|---|---|---|
| Surface homogeneity ($f_{dom}$) | $f_{dom} \geq 0.65$ | $0.50 \leq f_{dom} < 0.65$ | $0.35 \leq f_{dom} < 0.50$ | $f_{dom} < 0.35$ |
| Angular sampling ($f_{ang}$) | $f_{ang} \geq 0.60$ | $0.45 \leq f_{ang} < 0.60$ | $0.30 \leq f_{ang} < 0.45$ | $f_{ang} < 0.30$ |
| SZA | SZA ≤ 65° | 65° < SZA ≤ 72° | 72° < SZA ≤ 80° | SZA > 80° |
| VZA | VZA ≤ 55° | 55° < VZA ≤ 62° | 62° < VZA ≤ 70° | VZA > 70° |

Here, $f_{dom}$ is the areal fraction of the dominant MCD12Q1 IGBP class within the valid classified portion of a pixel. A pixel dominated by the MCD12Q1 water class is outside the land-surface scope of the database and is assigned $QA_0$. The angular-sampling fraction is:

$$f_{\mathrm{ang}} = \frac{N_{\mathrm{valid}}}{N_{\mathrm{nominal}}} \quad (S6)$$

Here, $N_{valid}$ and $N_{nominal}$ are the numbers of physically valid and nominal viewing directions, respectively. DPC-2 has 17 nominal directions. The minimum valid-direction counts corresponding to $QA_3$, $QA_2$, and $QA_1$ are 11, 8, and 6. POLDER-3 has 12 nominal directions, with corresponding minimum counts of 8, 6, and 4.

### S3.2 Sequence and direction grades

The atmospheric, surface-homogeneity, and angular-sampling grades define the quality of a complete multi-angle sequence:

$$\mathrm{Q_{seq}} = \min\left(\mathrm{Q_{atm}}, \mathrm{Q_{surf}}, \mathrm{Q_{ang}}\right) \quad (S7)$$

For viewing direction i, the geometry grade is

$$\mathrm{Q_{geo,i}} = \min\left(\mathrm{Q_{SZA,i}}, \mathrm{Q_{VZA,i}}\right) \quad (S8)$$

The direction-level grade is then

$$\mathrm{Q_{dir,i}} = \min\left(\mathrm{Q_{seq}}, \mathrm{Q_{geo,i}}\right) \quad (S9)$$

### S3.3 Band availability and Overall QA

Let $B_i$ denote the subset of the 490, 670, and 865 nm bands retained for direction i with positive weights. Each retained band inherits the direction-level grade:

$$\mathrm{Q_{AC,b,i}} = \mathrm{Q_{dir,i}} \quad (\mathrm{b} \in \mathrm{B_i}) \quad (S10)$$

A band that was missing or rejected was excluded from the final assignment rather than counted as $QA_0$. Because the fused $R_p$ required at least two retained bands, overall QA was assigned only when at least two valid bands remained. A missing individual band did not lower the grade derived from the remaining bands, provided that at least two bands were retained for fusion.

$$\mathrm{Q_{overall,i}} = \mathrm{Q_{dir,i}} \quad (|\mathrm{B_i}| \geq 2) \quad (S11)$$

If fewer than two bands were retained for direction i, no fused $R_p$ was available and overall QA was assigned $QA_0$. The quality grades of the participating bands were propagated using the same band-participation mask and relative weights as those used in the $R_p$ fusion. When the participating bands had identical sequence-level and geometry-level grades, weighting did not alter the resulting QA class. The validity criteria used to determine band participation are described in Sect. S2. In the QA summaries, band fusion denotes the quality grade propagated from the bands participating in the final $R_p$ fusion. Band coverage describes the amount of spectral support provided by the retained bands. Band coverage was treated as a diagnostic component rather than an independent constraint on overall QA.

## S4. Cross-sensor matching strategy

The matching unit was an individual viewing direction. A multi-angle sequence could contribute more than one matchup through different directions. Pixel location, dominant IGBP class, and NDVI were defined at the observation-sequence level and assigned to every directional observation within that sequence. Each candidate directional observation was required to have valid pixel-location, IGBP, SZA, VZA, RAA, NDVI, and $R_p$. Matching was performed separately for common dominant IGBP classes. Water Bodies were excluded. Candidate matchups had to satisfy:

$$d_{\mathrm{centre}} \leq 3\mathrm{km};\ |\Delta\mathrm{SZA}| \leq 0.5°;\ |\Delta\mathrm{VZA}| \leq 0.5°;\ |\Delta\mathrm{RAA}| \leq 1.0°;\ |\Delta\mathrm{NDVI}| \leq 0.020 \quad (S12)$$

Candidate search used a k-d tree constructed from threshold-normalized SZA, VZA, RAA, NDVI, and three-dimensional unit-sphere coordinates. At most the nearest 64 candidates in this joint space were checked against the original thresholds. Nearest admissible neighbours were identified independently from POLDER-3 to DPC-2 and from DPC-2 to POLDER-3, and only reciprocal matches were retained. The procedure therefore produced one-to-one pairs but was not a global assignment algorithm. The resulting pairs were used to assess conditional cross-sensor consistency under similar observed conditions rather than to validate either database against surface truth.

## S5. Semi-empirical BPDF model fitting

### S5.1 Semi-empirical BPDF models

In this study, we adopted several representative BPDF models proposed in previous studies for intercomparison. These models differ in their treatment of Fresnel reflection, geometric attenuation, shadowing effects, and vegetation dependence. Throughout Sect. S5, $\theta_{\mathrm{s}}$ and $\theta_{\mathrm{v}}$ denote the solar and viewing zenith angles, $\phi_{\mathrm{s}}$ and $\phi_{\mathrm{v}}$ denote the solar and viewing azimuth angles, $F_{\mathrm{p}}$ denotes the polarized Fresnel-reflection term, $\theta_{\mathrm{ia}}$ denotes the incidence angle associated with specular reflection, and $f_{\mathrm{sh}}$ denotes the model-specific shadowing function.

#### S5.1.1 Nadal model

Nadal and Bréon developed a semi-empirical model to describe polarized surface reflectance using a Fresnel-based polarization term combined with observation geometry (Nadal and Breon, 1999).

$$R_{\mathrm{p}} = p_{\mathrm{N},1}\left(1 - \exp\left(-\frac{p_{\mathrm{N},2}F_{\mathrm{p}}}{\cos(\theta_{\mathrm{s}}) + \cos(\theta_{\mathrm{v}})}\right)\right) \quad (S13)$$

where $p_{\mathrm{N},1}$ and $p_{\mathrm{N},2}$ are two free parameters. This model was derived from POLDER measurements and has been used for aerosol retrieval over land.

#### S5.1.2 Waquet model

Waquet further extended the Fresnel-based formulation developed by Nadal and Bréon by explicitly accounting for the mutual shadowing of surface facets (Waquet et al., 2009). The model was developed from airborne MICROPOL measurements over vegetated surfaces and introduces shadowing corrections for both the solar and viewing directions (Waquet et al., 2007).

$$R_{\mathrm{p}} = p_{\mathrm{W},1}F_{\mathrm{p}}S_{\mathrm{s}}S_{\mathrm{v}} \quad (S14)$$

with

$$v_{\mathrm{s}} = \frac{1}{p_{\mathrm{W},2}\sqrt{2}}\tan(\theta_{\mathrm{s}}),\ v_{\mathrm{v}} = \frac{1}{p_{\mathrm{W},2}\sqrt{2}}\tan(\theta_{\mathrm{v}}) \quad (S15)$$

$$S_{\mathrm{s}} = \frac{2}{1 + \mathrm{erf}(v_{\mathrm{s}}) + \sqrt{\pi}v_{\mathrm{s}}e^{-v_{\mathrm{s}}^2}},\ S_{\mathrm{v}} = \frac{2}{1 + \mathrm{erf}(v_{\mathrm{v}}) + \sqrt{\pi}v_{\mathrm{v}}e^{-v_{\mathrm{v}}^2}} \quad (S16)$$

This model contains two free parameters, $p_{\mathrm{W},1}$ and $p_{\mathrm{W},2}$. $p_{\mathrm{W},1}$ controls the overall magnitude of polarized surface reflectance, whereas $p_{\mathrm{W},2}$ is related to the mean square slope value and therefore characterizes surface roughness.

### S5.1.3 Maignan model

Maignan proposed a simplified one-parameter BPDF model for natural surfaces based on theoretical considerations and empirical fitting to POLDER-3 measurements (Maignan et al., 2009). Relative to earlier Fresnel-based formulations assuming random leaf orientation (Breon et al., 1995), this model introduces an explicit attenuation term associated with vegetation cover through NDVI, while retaining a compact analytical form.

$$R_{\mathrm{p}} = \frac{p_{\mathrm{M}} e^{-\tan(\theta_{\mathrm{ia}})} e^{-NDVI} F_{\mathrm{p}}}{4(\cos(\theta_{\mathrm{s}}) + \cos(\theta_{\mathrm{v}}))} \tag{S17}$$

This compact formulation contains one free parameter, $p_{\mathrm{M}}$, and it has been widely used in aerosol retrieval studies.

### S5.1.4 Diner model

Diner proposed a semi-empirical BPDF model for grass surfaces based on ground-based GroundMSPI measurements (Diner et al., 2012). This model assumes that reflecting facets are uniformly distributed and uses an explicit geometric description of the local facet orientation involved in specular reflection.

$$R_{\mathrm{p}} = \frac{p_{\mathrm{D}} F_{\mathrm{p}}}{8\pi \cos(\theta_{\mathrm{s}}) \cos(\theta_{\mathrm{v}}) \delta} \tag{S18}$$

where

$$\mathbf{n}_{\mathrm{s}} = \begin{bmatrix} \sin(\theta_{\mathrm{s}}) \cos\phi_{\mathrm{s}} \\ \sin(\theta_{\mathrm{s}}) \sin\phi_{\mathrm{s}} \\ \cos(\theta_{\mathrm{s}}) \end{bmatrix}, \mathbf{n}_{\mathrm{v}} = \begin{bmatrix} \sin(|\theta_{\mathrm{v}}|) \cos\phi_{\mathrm{v}} \\ \sin(|\theta_{\mathrm{v}}|) \sin\phi_{\mathrm{v}} \\ \cos(\theta_{\mathrm{v}}) \end{bmatrix} \tag{S19}$$

$$u_{\mathrm{n}} = \frac{(\mathbf{n}_{\mathrm{s}} + \mathbf{n}_{\mathrm{v}})_z}{\|\mathbf{n}_{\mathrm{s}} + \mathbf{n}_{\mathrm{v}}\|} \tag{S20}$$

$$\delta = \frac{\cos(\theta_{\mathrm{s}}) + \cos(\theta_{\mathrm{v}})}{2u_{\mathrm{n}}} \tag{S21}$$

This model has one free parameter, $p_{\mathrm{D}}$.

### S5.1.5 Litvinov model

Litvinov further extended previous BPDF formulations by introducing a more comprehensive description of polarized reflection over rough surfaces (Litvinov et al., 2011). Built on Fresnel reflection from a Gaussian random rough surface, the model additionally accounts for shadowing effects and assumes that reflecting facets are distributed within a volume rather than restricted to an idealized surface.

$$R_{\mathrm{p}} = \frac{p_{\mathrm{L},1} \pi F_{\mathrm{p}}}{4u_{\mathrm{n}}(\cos(\theta_{\mathrm{s}}) + \cos(\theta_{\mathrm{v}}))} f f_{\mathrm{sh}}(p_{\mathrm{L},3}) \tag{S22}$$

where

$$f = \frac{1}{2\pi p_{\mathrm{L},2} u_{\mathrm{n}}^3} \exp\left(-\frac{1-u_{\mathrm{n}}^2}{2p_{\mathrm{L},2}u_{\mathrm{n}}^2}\right) \quad (S23)$$

This model contains three free parameters, $p_{\mathrm{L},1}$, $p_{\mathrm{L},2}$, and $p_{\mathrm{L},3}$, and is therefore more flexible but also more complex than the simpler formulations..

### S5.1.6 Xie-Cheng model

Xie proposed a simplified semi-empirical BPDF model for urban areas (Xie et al., 2017). Based on Fresnel polarization theory, the model retains the shadowing effect while introducing an NDVI-dependent exponential term to account for the influence of vegetation cover on polarized surface reflectance.

$$R_{\mathrm{p}} = p_{\mathrm{XC},1} F_{\mathrm{p}} f_{\mathrm{sh}}\left(p_{\mathrm{XC},2}\right) e^{-w \cdot NDVI} \quad (S24)$$

where $w$ is fixed at 0.7. The analysis of Xie et al. (2017) suggested that the influence of the slope distribution is relatively weak for the considered urban surfaces, so that only two free parameters are needed, $p_{\mathrm{XC},1}$ and $p_{\mathrm{XC},2}$, one controlling the overall magnitude and the other describing the shadowing effect.

## S5.2 Parameter fitting of the semi-empirical BPDF models

A direction was considered physically valid for this comparison when $0 < R_{\mathrm{p}} < 1$. The model comparison was then restricted to sequences with valid Rp at all 17 DPC-2 or all 12 POLDER-3 viewing positions.

Each model was fitted independently to every retained multi-angle observation sequence.

$$\widehat{\boldsymbol{\theta}} = \arg\min_{\theta} \sum_{j \in \Omega} \left[R_{\mathrm{p,j}}^{\mathrm{obs}} - R_{\mathrm{p,j}}^{\mathrm{model}}\right]^2 \quad (S25)$$

where $R_{\mathrm{p,j}}^{\mathrm{obs}}$ and $R_{\mathrm{p,j}}^{\mathrm{model}}$ denote the observed and modelled polarized reflectances at viewing position j, respectively, Ω contains the viewing positions included in the fit.

Optimization was performed using the curve_fit function in SciPy. All included directional observations received equal weight. Because no initial parameter values were supplied, each free parameter was initialized to 1, and the unconstrained Levenberg–Marquardt algorithm was used. A fit was retained only when the optimizer returned the expected number of parameters and all fitted parameters and modelled values were finite.

## S5.3 Performance statistics of the semi-empirical BPDF models

Table S2. Performance of the semi-empirical BPDF models for DPC-2 and POLDER-3.

| DPC-2 | | | |
|---|---|---|---|
| Model | R | $R^2$ | RMSE ($\times 10^{-3}$) |

| | | | |
|---|---|---|---|
| Nadal | 0.8769 (0.0410) | **0.7328 (0.1015)** | 2.1346 (0.6530) |
| Waquet | 0.8218 (0.0613) | 0.5556 (0.1855) | 2.7561 (0.9927) |
| Diner | 0.7849 (0.0767) | 0.3075 (0.3530) | 3.2609 (0.8046) |
| Maignan | 0.8067 (0.0604) | 0.5540 (0.1693) | 2.7824 (0.9709) |
| Litvinov | 0.8616 (0.0674) | 0.7023 (0.1541) | **2.1187 (0.3876)** |
| Xie-Cheng | **0.8880 (0.0343)** | 0.7297 (0.1018) | 2.1676 (0.7342) |

**POLDER-3**

| Model | R | $R^2$ | RMSE ($\times 10^{-3}$) |
|---|---|---|---|
| Nadal | 0.9060 (0.0223) | 0.8161 (0.0437) | 1.8058 (0.2795) |
| Waquet | 0.8647 (0.0467) | 0.6793 (0.1507) | 2.3037 (0.4119) |
| Diner | 0.8366 (0.0524) | 0.4151 (0.2434) | 3.1038 (0.5946) |
| Maignan | 0.8358 (0.0483) | 0.6473 (0.1140) | 2.4742 (0.4773) |
| Litvinov | **0.9139 (0.0253)** | **0.8207 (0.0585)** | **1.7439 (0.1263)** |
| Xie-Cheng | 0.9117 (0.0190) | 0.8193 (0.0428) | 1.7924 (0.3002) |

Note: R, $R^2$, and RMSE are reported as the mean across viewing-angle positions, with the standard deviation across viewing angles given in parentheses. DPC-2 statistics are based on 17 viewing-angle positions, whereas POLDER-3 statistics are based on 12 viewing positions. RMSE is expressed in units of $\times 10^{-3}$. Bold values indicate the best performance for each sensor and metric.

## S6. Mixing-index analysis and sampling uncertainty

### S6.1 Valid pixel population and descriptive distributions

The sensor-specific empirical cumulative distributions of MI and the dominant-class-specific mean values were calculated from all valid observation sequences. For the descriptive relationship between MI and $R_{\mathrm{p}}$, each observation sequence was represented by the median of its valid directional $R_{\mathrm{p}}$ values and was required to contain at least three valid directions.

**S6.2 Mean MI differences**

Let c denote a dominant International Geosphere–Biosphere Programme (IGBP) land-cover class. The between-sensor difference in mean MI for class c was defined as:

$$\Delta \mathrm{MI_c} = \mathrm{MI_{DPC,c}} - \mathrm{MI_{POLDER,c}} \quad (S26)$$

Here, $\mathrm{MI_{DPC,c}}$ and $\mathrm{MI_{POLDER,c}}$ denote the mean MI values for class c in the DPC-2 and POLDER-3 databases, respectively. All valid records received equal weight. Longitude and latitude were transformed to the EPSG:6933 equal-area coordinate system and divided into 100 × 100 km spatial cells. Acquisition date and spatial cell defined the two clustering dimensions.

For the record-weighted mean of a generic variable y, the one-way cluster-robust variance associated with clustering dimension $g$ was estimated as:

$$V_{\mathrm{g}}(\overline{y}) = \frac{G_{\mathrm{g}}}{G_{\mathrm{g}} - 1} \frac{\sum_{k=1}^{G_{\mathrm{g}}} (S_{\mathrm{k}} - n_{\mathrm{k}}\overline{y})^2}{N^2} \quad (S27)$$

where $G_{\mathrm{g}}$ is the number of clusters, $n_{\mathrm{k}}$ and $S_{\mathrm{k}}$ are the number and sum of observations in cluster k, and $N$ is the total number of records.

The two one-way variance estimates were combined using the two-way cluster-robust inclusion–exclusion estimator:

$$\hat{V}_{\mathrm{2way}} = \hat{V}_{\mathrm{data}} + \hat{V}_{\mathrm{space}} - V_{\mathrm{date \cap space}} \quad (S28)$$

Any negative numerical value produced by the two-way variance estimator was truncated to zero. The two sensor means were treated as independent. The standard error of their difference was therefore calculated as:

$$SE(\Delta \mathrm{MI_c}) = \sqrt{\hat{V}_{\mathrm{DPC},c} + \hat{V}_{\mathrm{POLDER},c}} \quad (S29)$$

The reference degrees of freedom were the smallest relevant date or spatial cluster count across the two sensors minus one. Two-sided 95% confidence intervals and P values were calculated from the corresponding Student t distribution. For the class-specific comparisons, the resulting P values were adjusted using the Benjamini–Hochberg procedure to control the false-discovery rate across the tested IGBP classes. The adjusted values are reported as q values.

**S6.3 Geometry-adjusted MI effects**

The analysis of observation geometry used a fixed-seed uniform-priority reservoir containing at most 400,000 directions for each sensor-wide model and at most 50,000 directions for each sensor-IGBP model. Each class-specific model required at least 200 directional observations, 30 pixels, and non-zero variation in MI. Classes not meeting these conditions or producing an unidentified coefficient were omitted rather than plotted as zero effects. Linear and quadratic geometry terms were included because the response of $R_{\mathrm{p}}$ to solar and viewing geometry is generally nonlinear. Their inclusion reduces interference from differences in observation geometry when estimating the association between MI and $R_{\mathrm{p}}$.

For direction v from pixel i, the geometry-adjusted model was:

$$R_{\mathrm{p,i,v}} = \alpha + \beta \mathrm{MI_i} + \sum_{g\in\{\mathrm{SZA,VZA,RAA}\}} (\gamma_{\mathrm{g}} z_{\mathrm{g,i,v}} + \delta_{\mathrm{g}} z^2_{\mathrm{g,i,v}}) + \varepsilon_{\mathrm{i,v}} \quad (S30)$$

Here, $z_g$ is the standardized geometry variable within each fitted model. The parameter $\alpha$ is the intercept, and $\beta$ is the partial regression coefficient for MI before the reporting-scale transformation described below. The parameters $\gamma_{\mathrm{g}}$ and $\delta_{\mathrm{g}}$ are the corresponding linear and quadratic geometry coefficients, and $\varepsilon_{\mathrm{i,v}}$ is the regression residual. Thus, $\beta$ describes the association between MI and surface polarized reflectance after adjustment for the modelled geometry effects.

The sensor-wide models additionally included fixed effects for the dominant IGBP class. Class-specific models were fitted separately for each sensor and class.

Each directional observation received the weight:

$$w_{\mathrm{i,v}} = \frac{1}{n_{\mathrm{i}}} \quad (S31)$$

where $n_{\mathrm{i}}$ is the number of valid directions contributed by pixel i. Thus, the total nominal weight of each pixel was approximately one.

For each clustering dimension, the corresponding one-way cluster-robust covariance matrix was multiplied by the finite-sample correction factor:

$$\frac{G}{G-1}\frac{n-1}{n-p} \quad (S32)$$

where G is the number of clusters in the clustering dimension under consideration, n is the number of regression rows, and p is the number of fitted model parameters, including the intercept and all applicable MI, geometry, and land-cover terms.

The date-, space-, and date-by-space covariance matrices were combined as in Eq. (S28). Degrees of freedom were

$$\nu = \min\left(G_{\mathrm{date}}, G_{\mathrm{space}}\right) - 1 \quad (S33)$$

Two-sided 95% confidence intervals and P values were calculated from the Student t distribution with these degrees of freedom. The estimated MI coefficient and both confidence limits were multiplied by 0.1, so the reported effect represents the change in $R_p$ associated with a 0.1-unit increase in MI.

**S7. File structure of the public BPDF databases**

Each BPDF database is distributed as one complete CSV file and a set of monthly CSV files. The monthly files are named DPC-2_YYYY_MM.csv and POLDER-3_YYYY_MM.csv. Here, YYYY is the four-digit acquisition year and MM is the two-digit acquisition month. The complete and monthly files for a given sensor have the same column structure. The first row of each file contains the field names. Each subsequent row represents one multi-angle observation sequence for a satellite pixel acquired on a single date. The fields are organized into sequence-level information followed by eight blocks of direction-specific information. The DPC-2 files contain 143 columns, while the POLDER-3 files contain 103 columns. Their exact column structures are given in Table S3.

For DPC-2, i takes integer values from 0 to 16. Each direction-specific block therefore contains 17 fields. For example, the SZA block begins with SZA_0 in column 8 and ends with SZA_16 in column 24. The same indexing rule applies to the VZA, RAA, band-specific polarized-reflectance, fused polarized-reflectance, and quality-assurance fields. For POLDER-3, i takes integer values from 0 to 11. Each direction-specific block therefore contains 12 fields. For example, the SZA block begins with SZA_0 in column 8 and ends with SZA_11 in column 19. The same indexing rule applies to all subsequent direction-specific blocks.

A common direction index links the geometry, band-specific surface polarized reflectances, fused polarized reflectance, and quality-assurance grade belonging to the same directional observation. Thus, SZA_i, VZA_i, RAA_i, Rp_490_i, Rp_670_i, Rp_865_i, Rp_i, and qa_overall_i all refer to viewing direction i within the same observation sequence. The band-specific and fused polarized-reflectance fields are dimensionless. The qa_overall_i field contains an integer value from 0 to 3, corresponding to grades $QA_0$ to $QA_3$. Higher qa_overall_i values indicate greater internal reliability according to the QA framework described in Sect. S3. An empty CSV field indicates that no valid numerical value is available for the corresponding variable and viewing direction.

**Table S3 Column structure of the public POLDER-3 and DPC-2 BPDF database files.**

| Field | DPC-2 column positions | POLDER-3 column positions | Description |
|---|---|---|---|
| Year | 1 | 1 | Acquisition year |
| Month | 2 | 2 | Acquisition month |
| Day | 3 | 3 | Acquisition day |
| Lat | 4 | 4 | Latitude of the pixel centre in degrees |
| Lon | 5 | 5 | Longitude of the pixel centre in degrees |
| HEIGHT | 6 | 6 | Surface elevation in kilometres |
| IGBP | 7 | 7 | Dominant IGBP land-cover class |
| SZA_i | 8–24 | 8–19 | Solar zenith angle for viewing direction i, in degrees |
| VZA_i | 25–41 | 20–31 | Viewing zenith angle for viewing direction i, in degrees |
| RAA_i | 42–58 | 32–43 | Relative azimuth angle for viewing direction i, in degrees |
| Rp_490_i | 59–75 | 44–55 | Atmospherically corrected surface polarized reflectance at 490 nm for viewing direction i |
| Rp_670_i | 76–92 | 56–67 | Atmospherically corrected surface polarized reflectance at 670 nm for viewing direction i |
| Rp_865_i | 93–109 | 68–79 | Atmospherically corrected surface polarized reflectance at 865 nm for viewing direction i |

| | | | |
|---|---|---|---|
| Rp_i | 110–126 | 80–91 | Surface polarized reflectance obtained by multiband fusion for viewing direction i |
| qa_overall_i | 127–143 | 92–103 | Overall quality-assurance grade for viewing direction i |

**S8. Statistical metrics**

$$R = \frac{\sum_{i=1}^{n}( x_{\mathrm{i}} - \bar{x})(y_{\mathrm{i}} - \bar{\mathrm{y}})}{\sqrt{\sum_{i=1}^{n}( x_{\mathrm{i}} - \bar{\mathrm{x}})^2 \sum_{i=1}^{n}( y_{\mathrm{i}} - \bar{\mathrm{y}})^2}} \quad (S34)$$

$$RMSE = \sqrt{\frac{1}{n}\sum_{i=1}^{n}( x_{\mathrm{i}} - y_{\mathrm{i}})^2} \quad (S35)$$

$$Bias = \frac{1}{n}\sum_{i=1}^{n}( x_{\mathrm{i}} - y_{\mathrm{i}}) \quad (S36)$$

Here, $x_{\mathrm{i}}$ and $y_{\mathrm{i}}$ denote the paired values being compared, $n$ is the number of valid pairs, and $\bar{x}$ and $\bar{y}$ are their corresponding means. The sign of Bias follows the order $x_{\mathrm{i}} - y_{\mathrm{i}}$. For the cross-sensor comparison, $x_{\mathrm{i}}$ denotes DPC-2 $R_{\mathrm{p}}$ and $y_{\mathrm{i}}$ denotes POLDER-3 $R_{\mathrm{p}}$, so a positive Bias indicates a higher DPC-2 value.

**References**


Breon, F.-M., Tanre, D., Lecomte, P., and Herman, M.: Polarized reflectance of bare soils and vegetation: measurements and models, IEEE Trans. Geosci. Remote Sensing, 33, 487–499, https://doi.org/10.1109/TGRS.1995.8746030, 1995.

Diner, D. J., Xu, F., Martonchik, J. V., Rheingans, B. E., Geier, S., Jovanovic, V. M., Davis, A., Chipman, R. A., and McClain, S. C.: Exploration of a Polarized Surface Bidirectional Reflectance Model Using the Ground-Based Multiangle SpectroPolarimetric Imager, Atmosphere, 3, 591–619, https://doi.org/10.3390/atmos3040591, 2012.

Litvinov, P., Hasekamp, O., and Cairns, B.: Models for surface reflection of radiance and polarized radiance: Comparison with airborne multi-angle photopolarimetric measurements and implications for modeling top-of-atmosphere measurements, Remote Sensing of Environment, 115, 781–792, https://doi.org/10.1016/j.rse.2010.11.005, 2011.

Maignan, F., Bréon, F.-M., Fédèle, E., and Bouvier, M.: Polarized reflectances of natural surfaces: Spaceborne measurements and analytical modeling, Remote Sensing of Environment, 113, 2642–2650, https://doi.org/10.1016/j.rse.2009.07.022, 2009.

Nadal, F. and Breon, F.-M.: Parameterization of surface polarized reflectance derived from POLDER spaceborne measurements, IEEE Trans. Geosci. Remote Sensing, 37, 1709–1718, https://doi.org/10.1109/36.763292, 1999.

Omar, A. H., Won, J.-G., Winker, D. M., Yoon, S.-C., Dubovik, O., and McCormick, M. P.: Development of global aerosol models using cluster analysis of Aerosol Robotic Network (AERONET) measurements, Journal of Geophysical Research: Atmospheres, 110, https://doi.org/https://doi.org/10.1029/2004JD004874, 2005.

Waquet, F., Goloub, P., Deuzé, J. -L., Léon, J. -F., Auriol, F., Verwaerde, C., Balois, J. -Y., and François, P.: Aerosol retrieval over land using a multiband polarimeter and comparison with path radiance method, J. Geophys. Res., 112, 2006JD008029, https://doi.org/10.1029/2006JD008029, 2007.

Waquet, F., Léon, J.-F., Cairns, B., Goloub, P., Deuzé, J.-L., and Auriol, F.: Analysis of the spectral and angular response of the vegetated surface polarization for the purpose of aerosol remote sensing over land, Appl. Opt., 48, 1228–1236, https://doi.org/10.1364/AO.48.001228, 2009.

Xie, D., Cheng, T., Wu, Y., Fu, H., Zhong, R., and Yu, J.: Polarized reflectances of urban areas: Analysis and models, Remote Sensing of Environment, 193, 29–37, https://doi.org/https://doi.org/10.1016/j.rse.2017.02.026, 2017.